

Unrevealing the existence of nontensorial gravitational-wave polarizations from individual supermassive black hole binaries with pulsar timing arrays

Dicong Liang,^{1,2,*} Siyuan Chen,^{1,3} Chao Zhang,⁴ and Lijing Shao^{1,5,†}

¹*Kavli Institute for Astronomy and Astrophysics, Peking University, Beijing 100871, China*

²*Department of Mathematics and Physics, School of Biomedical Engineering,
Southern Medical University, Guangzhou 510515, China*

³*Shanghai Astronomical Observatory, Chinese Academy of Sciences, Shanghai 200030, China*

⁴*School of Aeronautics and Astronautics, Shanghai Jiao Tong University, Shanghai 200240, China*

⁵*National Astronomical Observatories, Chinese Academy of Sciences, Beijing 100012, China*

With the strong evidence for a gravitational wave (GW) background in the nanohertz frequency band from pulsar timing arrays, the detection of continuous GWs from individual supermassive black hole binaries is already at the dawn. Utilizing continuous GWs to test theories of gravity, especially to test the polarizations of GWs is becoming more and more realistic. In this theoretical study, assuming a detection of signals from individual supermassive binary black holes, we use the null stream to estimate the capability of identifying the nontensorial polarizations of GWs. We consider cases for the nontensorial polarizations where the dipole radiation and quadrupole radiation dominate separately. With a frequentist method, we estimate the threshold of the nontensor-to-tensor relative amplitude above which extra polarizations can be detected. We also conduct Bayesian analysis to do parameter estimation with the null stream data. Our treatment provides a data-analysis methodology using the null stream to probe the nontensorial GW polarizations with pulsar timing arrays.

I. INTRODUCTION

Recently, evidence for a gravitational wave (GW) background was found by several pulsar timing array (PTA) collaborations, which are the North American Nanohertz Observatory for Gravitational Waves (NANOGrav) [1], the European Pulsar Timing Array (EPTA) [2], the Parkes Pulsar Timing Array (PPTA) [3], and the Chinese Pulsar Timing Array (CPTA) [4]. The detection of GWs by PTAs will enable us to probe new physics encoded in the nanohertz GWs [5–14].

As an important property of GWs, the polarization content can be used to test gravity theories. There can be up to six polarizations in general metric gravity theories [15, 16]. In addition to the two tensor polarizations in general relativity, there can be scalar polarizations and vector polarizations in modified gravity theories [17–19]. The response of a PTA to the nontensorial polarizations and the corresponding overlap reduction function in the GW background (GWB) search were discussed in a general framework in Refs. [20–24], and were studied in some specific theories [25–28]. Forecasts on constraining extra polarizations with GWB signals were widely studied in literature [29, 30]. Recent analysis on the real dataset from NANOGrav suggests that the possibility of the existence of the breathing mode cannot be excluded [31, 32].

Continuous GWs emitted from an individual supermassive binary black hole (SMBBH) is another important target signal for PTAs [5, 33–37], and GWs from the loudest signals from individual SMBBHs are expected to

be detected following the detection of GWB [35]. Current data provide no evidence of such a signal [38, 39]. Nevertheless, there are a few studies on constraining the extra polarizations of GWs from individual SMBBHs [40, 41].

For the GW detection in the audio frequency band at $\sim 10^2$ Hz, the Bayesian model selection is generally used to do the polarization tests [42–46]. At the same time, the null stream method has been developed to probe the existence of nontensorial polarizations for the ground-based GW detector network and space-based GW detectors [47–53]. Null streams can be constructed by the special linear combination of the multiple data streams from the detector network, such that the tensorial signals are completely eliminated [54–56]. Based on this idea, there are also some studies on using null stream to localize the source in the PTA community [57–60]. In this work, for the first time we utilize the null streams to estimate the detectability of nontensorial GWs with PTAs, which provides a strategy in using the null stream to probe the nontensorial GW polarizations for future real data analysis. Throughout the paper, we only consider one GW source for each simulation.

The paper is organized as follows. In Sec. II, we introduce some basic concepts about extra polarizations, the waveform models, and the way to construct null streams. Next, we estimate the sensitivity of PTAs to the extra polarization and obtain the detection threshold of the nontensor-to-tensor relative amplitude with a frequentist method in Sec. III. Then we use the null stream to estimate the parameters with Bayesian inference in Sec. IV. Final discussions are presented in Sec. V.

* Corresponding author: dcliang@pku.edu.cn

† Corresponding author: lishao@pku.edu.cn

II. METHODOLOGY

In this section we provide the settings used in this work, including the extra GW polarizations in PTAs in Sec. II A, GW waveforms in Sec. II B, and the null stream in Sec. II C.

A. Extra polarizations

We first introduce the orthonormal coordinate system

$$\begin{aligned}\hat{\Omega} &= (\sin \theta \cos \phi, \sin \theta \sin \phi, \cos \theta), \\ \hat{\mathbf{m}} &= (\cos \theta \cos \phi \cos \psi - \sin \phi \sin \psi, \\ &\quad \cos \theta \sin \phi \cos \psi + \cos \phi \sin \psi, -\sin \theta \cos \psi), \\ \hat{\mathbf{n}} &= (-\cos \theta \cos \phi \sin \psi - \sin \phi \cos \psi, \\ &\quad -\cos \theta \sin \phi \sin \psi + \cos \phi \cos \psi, \sin \theta \sin \psi),\end{aligned}\quad (1)$$

where θ and ϕ denote the propagation direction of the GWs (i.e. $-\hat{\Omega}$ points towards the GW source), and ψ is the polarization angle. Then the basic tensors for the six polarizations (denoted as ‘+’, ‘ \times ’, ‘ x ’, ‘ y ’, ‘ b ’, ‘ l ’) are

$$\begin{aligned}e_{ij}^+ &= \hat{m}_i \hat{m}_j - \hat{n}_i \hat{n}_j, & e_{ij}^\times &= \hat{m}_i \hat{n}_j + \hat{n}_i \hat{m}_j, \\ e_{ij}^x &= \hat{m}_i \hat{\Omega}_j + \hat{\Omega}_i \hat{m}_j, & e_{ij}^y &= \hat{n}_i \hat{\Omega}_j + \hat{\Omega}_i \hat{n}_j, \\ e_{ij}^b &= \hat{m}_i \hat{m}_j + \hat{n}_i \hat{n}_j, & e_{ij}^l &= \hat{\Omega}_i \hat{\Omega}_j.\end{aligned}\quad (2)$$

We only consider the case where all the possible polarizations propagate at the speed of light and are monochromatic. Then, the timing residuals r_A of a pulsar induced by polarization A are given by

$$r_A = F_A h_A, \quad (3)$$

with the strain h_A and the response function F_A [61, 62]

$$F_A = \frac{1}{4\pi i f_A} \frac{\hat{p}^i \hat{p}^j e_{ij}^A(\hat{\Omega})}{1 + \hat{\Omega} \cdot \hat{\mathbf{p}}} \left[1 - e^{-i2\pi f_A L_p (1 + \hat{\Omega} \cdot \hat{\mathbf{p}})/c} \right]. \quad (4)$$

Here $\hat{\mathbf{p}}$ is the unit vector pointing in the direction to the pulsar, L_p is the distance between the pulsar and the Earth, f_A is the frequency of the GW polarization mode A . Even for a circular binary, the extra polarizations can have different frequency evolution from the tensor polarizations [56]. We also define the combined response to the tensor and vector modes as $|F_t|^2 \equiv |F_+|^2 + |F_\times|^2$, and $|F_v|^2 \equiv |F_x|^2 + |F_y|^2$.

In this work, we consider $N = 49$ pulsars from the International Pulsar Timing Array data release 1 (IPTA-DR1) [63] and the distance of these pulsars are inquired from the Australia Telescope National Facility (ATNF) pulsar catalogue¹ [64].

As a theoretical study, for now we only consider the white Gaussian noise in the data and we further assume the timing residuals of all the pulsars have the same variance $\sigma_t = 100$ ns for simplicity. The overall angular response of these 49 pulsars to different polarizations, i.e., $|F_A|^2 = \sum_{i=1}^{49} |F_{i,A}|^2$, is shown in Fig. 1. The 49 pulsars are denoted with red stars in the figure. Here, we assume that the frequency of the extra polarizations is half of that of tensor polarizations, corresponding to the dipole radiation. To consider different timing residual variances we can get the response by a re-weighted summation of the response of each pulsar.

The most sensitive regions for the transverse modes (i.e., the tensor modes and the breathing mode) are the left hemisphere, where most of the pulsars are located. While the most sensitive region for the vector modes and the longitudinal mode are the “islands” surrounding each pulsar. It is because that the response gets boosted for these modes when the angular separation between the GW source and the pulsar is small [41]. Another important feature of the sensitivity skymap is that, the response oscillates quickly over the sky location due to the “pulsar term”, which is the second term in the square bracket in Eq. (4).

B. Waveform model

For the two tensor modes, we parameterize the waveform as follows

$$\begin{aligned}h_+ &= h_0 \frac{1 + \cos^2 \iota}{2} \exp[i(2\pi f_0 t + 2\Phi_0)], \\ h_\times &= -i h_0 \cos \iota \exp[i(2\pi f_0 t + 2\Phi_0)],\end{aligned}$$

where Φ_0 is the initial orbital phase of the binary, h_0 is the fiducial amplitude, which depends on the binary masses, frequency and luminosity distance. Throughout the paper, we adopt $f_0 = 20$ nHz and fix $h_0 = 10^{-14}$, which is a bit smaller than the current upper limit estimated by NANOGrav [38] and EPTA [39].

For the extra polarizations, we consider two cases. In the first case (Case 1), we assume the dipole emission dominates as in Ref. [41]. The parameterized waveforms are given by

$$\begin{aligned}h_x &= A_v h_0 \cos \iota \exp[i(\pi f_0 t + \Phi_0)], \\ h_y &= -i A_v h_0 \exp[i(\pi f_0 t + \Phi_0)], \\ h_b &= A_b h_0 \sin \iota \exp[i(\pi f_0 t + \Phi_0)], \\ h_l &= A_l h_0 \sin \iota \exp[i(\pi f_0 t + \Phi_0)].\end{aligned}\quad (5)$$

Here, A_v , A_b and A_l are the relative amplitudes for the vector mode, breathing mode and longitudinal mode respectively. Notice that, in this case, the frequency of the extra modes is only half of that of the tensor modes.

For the second case (Case 2), we assume that quadrupole radiation dominates. Then we follow Takeda

¹ <https://www.atnf.csiro.au/people/pulsar/psrcat/>

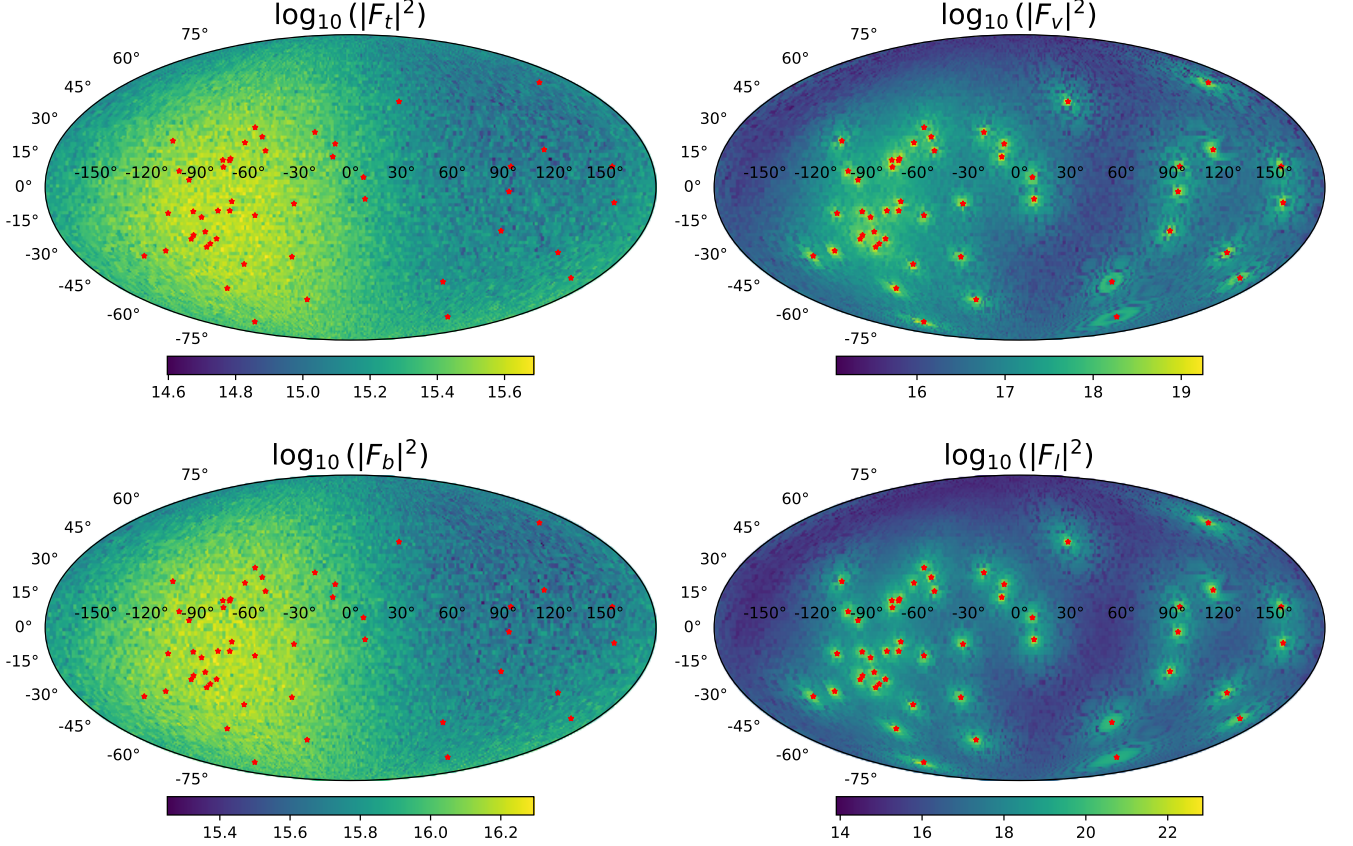


FIG. 1. The overall response of the 49 pulsars (denoted with red stars) at different sky locations. Here, we set the frequency of the tensor modes as 20 nHz while the frequency of all the other modes is 10 nHz.

et al. [65] to parameterize them as

$$\begin{aligned}
 h_x &= -A_v h_0 \frac{\sin 2\iota}{2} \exp[i(2\pi f_0 t + 2\Phi_0)], \\
 h_y &= iA_v h_0 \sin \iota \exp[i(2\pi f_0 t + 2\Phi_0)], \\
 h_b &= -A_b h_0 \frac{\sin^2 \iota}{2} \exp[i(2\pi f_0 t + 2\Phi_0)], \\
 h_l &= A_l h_0 \frac{\sin^2 \iota}{2} \exp[i(2\pi f_0 t + 2\Phi_0)].
 \end{aligned} \tag{6}$$

In this case, all the extra polarizations have the same frequency as the tensor modes. Considering that f_A is in the denominator of the response function [see Eq. (4)], the response to the extra polarizations in Case 2 is weaker than that in Case 1. We can also notice that the dependence on the inclination angle is different between these two cases.

Following Goldstein *et al.* [59], we assume $N_{\text{TOA}} = 300$ times of arrival (TOAs), evenly distributed in time with a cadence of $\Delta t = 10^6$ s. Thus, the total observation time is around 9.5 years.

C. Null stream

Now we introduce how to construct a null stream [57]. In general relativity, we can write the 49 data streams in matrix as follows

$$\begin{pmatrix} \mathbf{d}_1 \\ \mathbf{d}_2 \\ \vdots \\ \mathbf{d}_N \end{pmatrix} = \begin{pmatrix} F_1^+ & F_1^\times \\ F_2^+ & F_2^\times \\ \vdots & \vdots \\ F_N^+ & F_N^\times \end{pmatrix} \begin{pmatrix} \mathbf{h}^+ \\ \mathbf{h}^\times \end{pmatrix} + \begin{pmatrix} \mathbf{n}_1 \\ \mathbf{n}_2 \\ \vdots \\ \mathbf{n}_N \end{pmatrix}, \tag{7}$$

or in a more compact form

$$\mathbf{d} = \mathbf{r} + \mathbf{n} = \mathbf{F}_t \mathbf{h}_t + \mathbf{n}, \tag{8}$$

where $\mathbf{F}_t = (\mathbf{F}^+, \mathbf{F}^\times)$. We perform the singular value decomposition for \mathbf{F}_t as in Ref. [57] to get

$$\mathbf{F}_t = \mathbf{U} \mathbf{S} \mathbf{V}^\dagger, \quad \mathbf{S} = \begin{pmatrix} s_1 & 0 \\ 0 & s_2 \\ 0 & 0 \\ \vdots & \vdots \\ 0 & 0 \end{pmatrix}, \tag{9}$$

where \mathbf{U} and \mathbf{V} are unitary matrices, s_1 and s_2 are the singular values and the symbol \dagger denotes conjugate transpose. Projecting the matrix \mathbf{U}^\dagger onto the original data streams, we finally obtain the new data streams

$$\tilde{\mathbf{d}} \equiv \mathbf{U}^\dagger \mathbf{d} = \begin{pmatrix} s_1(\mathbf{V}^\dagger \mathbf{h}_t)_1 + \tilde{\mathbf{n}}_1 \\ s_2(\mathbf{V}^\dagger \mathbf{h}_t)_2 + \tilde{\mathbf{n}}_2 \\ \tilde{\mathbf{n}}_3 \\ \vdots \\ \tilde{\mathbf{n}}_N \end{pmatrix}, \quad (10)$$

where $\tilde{\mathbf{n}} = \mathbf{U}^\dagger \mathbf{n}$. Now, the new data streams, \tilde{d}_k with $k \geq 3$, are the so-called null streams since they do not contain any tensorial signals. Notice that \mathbf{U} is a unitary matrix, which does not change the statistic property of the noise. In this work, we consider the statistic X related to the null streams, which is defined as

$$X = \sum_{k=3}^{49} \sum_n^{N_{\text{TOA}}} \frac{1}{\sigma_t^2} |\tilde{d}_k(t_n)|^2. \quad (11)$$

Considering white noise only, the statistic X follows a χ^2 distribution with degrees of freedom $N_{\text{dof}} = 47 \times N_{\text{TOA}}$.

Notice that the construction of these null streams needs precise knowledge of the response function matrix \mathbf{F}_t . It is an idealized assumption throughout the paper and we hope to relax it in the future study.

III. FREQUENTIST ANALYSIS

If there are extra polarizations, then the data streams can now be written as

$$\mathbf{d} = \mathbf{F}_t \mathbf{h}_t + \mathbf{F}_e \mathbf{h}_e + \mathbf{n}. \quad (12)$$

Here, the subscript e denotes any extra polarization. After the projection by \mathbf{U}^\dagger , the new tensor-polarization-null streams \mathbf{d}_k ($k \geq 3$) still contain the component $(\mathbf{U}^\dagger \mathbf{F}_e \mathbf{h}_e)_j$, i.e.,

$$\tilde{\mathbf{d}} = \begin{pmatrix} s_1(\mathbf{V}^\dagger \mathbf{h}_t)_1 + \tilde{\mathbf{n}}_1 + (\mathbf{U}^\dagger \mathbf{F}_e \mathbf{h}_e)_1 \\ s_2(\mathbf{V}^\dagger \mathbf{h}_t)_2 + \tilde{\mathbf{n}}_2 + (\mathbf{U}^\dagger \mathbf{F}_e \mathbf{h}_e)_2 \\ \tilde{\mathbf{n}}_3 + (\mathbf{U}^\dagger \mathbf{F}_e \mathbf{h}_e)_3 \\ \vdots \\ \tilde{\mathbf{n}}_N + (\mathbf{U}^\dagger \mathbf{F}_e \mathbf{h}_e)_N \end{pmatrix}. \quad (13)$$

In this case, X no longer follows the χ^2 distribution and the deviation can be significant if the extra polarization is strong enough. We assign a p -value to quantify its deviation from the χ^2 distribution, defined as

$$p = \int_X^\infty \chi_{N_{\text{dof}}}^2(x) dx. \quad (14)$$

As we can see in Fig. 1, the angular response is quickly oscillating over the sky location due to the existence of

the pulsar term. Thus, for the extra polarizations with the same amplitude, the effects on the TOA can vary significantly for GW sources at different sky locations. In other words, X can vary significantly for different sky locations. To check the average sensitivity of a PTA to the extra polarizations, we do some simulations by injecting the extra polarizations separately.

Specifically, we first draw $\cos \iota$ from uniform distribution $U[0, 1]$ and draw ψ and Φ_0 from uniform distribution $U[0, 2\pi)$. After fixing $\cos \iota$, ψ and Φ_0 , we simulate 10^4 uniformly spatial distributed sources, i.e., $\cos \theta$ follows uniform distribution $U[-1, 1]$ and ϕ follows uniform distribution $U[-\pi, \pi)$. Then, we calculate the p -value for these 10^4 random sources separately with the same relative amplitude A . Finally, we calculate the fraction F_N of the events whose $p < 1.35 \times 10^{-3}$, i.e.

$$F_N = \frac{N(p < 1.35 \times 10^{-3})}{10^4}. \quad (15)$$

We get the fraction F_N for a given A for different polarizations in each simulation. It is an estimation of the size of the fraction of the sky locations where we can detect extra polarizations with $> 3\sigma$ significance for the specific relative strength. It can also be interpreted as the probability of detecting nontensorial polarizations for a source randomly distributed on the sky.

We perform 200 simulations and the results are denoted with thin lines in Fig. 2 where different colors represent different injected polarizations. For the 10 choices of A , the median value of F_N of the 200 simulations are denoted as triangles in the figure. The variance is due to the different choices of ι , ψ and Φ_0 . Notice that we choose smaller amplitudes for simulations in Case 1 than that in Case 2, since the response is stronger in Case 1 than that in Case 2. In addition, the factor corresponding to the inclination in the waveform is larger in Case 1 than that in Case 2.

Overall, the fraction decreases when the relative amplitude gets smaller and the decline of the longitudinal mode is the slowest. The variance of the breathing mode is quite large here, since its strength strongly depends on the inclination. As shown in Fig. 1, the response at the brightest regions is so strong that it dominates the contribution to the strength. Thus, the effects of inclination are weaker for the longitudinal mode, although it has the same inclination dependence as the breathing mode.

Now, we extend our analysis to the cases with more pulsars. First, we follow Speri *et al.* [66] to create an array of 200 pulsars with Galaxy distribution on the sky. The distances of these pulsars follow a Gaussian distribution, whose mean and variance are the same as those of the 49 pulsars in IPTA-DR1. We choose 20 sets of relative amplitude uniformly and set ι , ψ and Φ_0 to be $\pi/3$ for all the GW sources. We again simulate 10^4 sources with different sky locations, and calculate the fraction. The results are shown in Fig. 3. The results of the 49 pulsars and 200 pulsars are denoted with solid lines and dotted lines respectively. Generally speaking, when $A > 0.125$

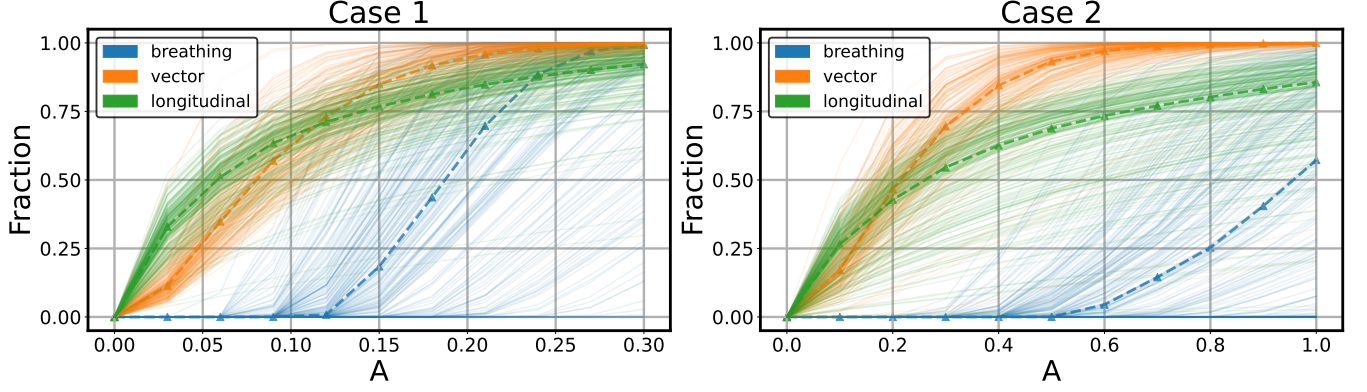


FIG. 2. The fraction of sky locations we can detect extra polarizations with $> 3\sigma$ confidence level at a given relative amplitude calculated for 200 simulations. Each thin line represents one simulation and the dotted line shows the median over the 200 simulations.

in Case 1 or $A > 0.65$ in Case 2, the breathing mode can be detected at 3σ level for almost all sky locations if there are 200 pulsars. For the vector and longitudinal modes, more pulsars mean more sensitive “islands”, leading to significant improvement for the sky coverage.

In above analysis, we perform the singular value decomposition for matrix $\mathbf{F}_t = (\mathbf{F}^+, \mathbf{F}^\times) = \mathbf{U}\mathbf{S}\mathbf{V}^\dagger$ to project out the tensor modes only. Thus, we can only know that there exist nontensorial polarizations if we find significant deviation between the null stream and noise, but we cannot tell which kind of extra polarizations are present. However, we can construct $\hat{\mathbf{U}}_b$ such that $(\mathbf{F}^+, \mathbf{F}^\times, \mathbf{F}^x, \mathbf{F}^y, \mathbf{F}^l) = \hat{\mathbf{U}}_b \mathbf{S}_b \mathbf{V}_b^\dagger$. Then we can get the new data streams $\tilde{\mathbf{d}}_b = \hat{\mathbf{U}}_b^\dagger \mathbf{d}$, where 44 of them contain only the breathing mode and the noise. Using the same method, we can obtain 45 data streams with only vector modes and 44 data streams with only longitudinal modes, in addition to the noise.

With these new null streams, we can define the injected SNR [41] as

$$\rho_{\text{inj}} = \sum_{k=\ell}^{49} \sum_n^{N_{\text{TOA}}} \frac{1}{\sigma_t^2} |\tilde{d}_{e,k}(t_n)|^2, \quad (16)$$

where $\ell = 4$ for the breathing and longitudinal modes, and $\ell = 5$ for the vector modes. If the SNR is large enough, we expect large deviation of the null stream from the noise and a corresponding extremely small p -value. In such a case we can claim a strong evidence for the existence of the specific extra polarizations.

Now, we want to estimate how large the relative amplitude should be to detect the specific extra polarizations. First, we generate a random source, whose angles, i.e. θ , ϕ , ι and Φ_0 have the same distribution as in the previous analysis. Then, we find the threshold value of A that corresponds to an injected SNR $\rho_{\text{inj}} = 22$, which is approximately equivalent to a 3σ confidence level. We generate 2×10^6 random sources, and the histogram of threshold A of these 2×10^6 simulations are shown in

Fig. 4. The dashed and solid lines represent the results for Case 1 and Case 2 respectively.

For randomly distributed sources, the median values for the relative amplitude to produce a signal with $\rho_{\text{inj}} = 22$ in the null streams are $A_b = 0.26$, $A_v = 0.13$, $A_l = 0.15$ for Case 1, and $A_b = 1.36$, $A_v = 0.37$, $A_l = 0.81$ for Case 2. As explained previously, the expected amplitude is smaller in Case 1 than that in Case 2, due to its inclination dependence in the waveform and frequency dependence in the angular response function. It should be noted that the variance of the relative amplitude of the longitudinal mode is very large. This is not surprising, as we can see in Fig. 1, that there can be up to seven orders of magnitude difference in the response function for the longitudinal mode.

IV. BAYESIAN ANALYSIS

In the previous section we have estimated the average sensitivity of PTAs to the extra polarizations and quantified the relative amplitude threshold for detection. Now, we study how well we can recover the parameters of signals of extra polarizations with the null streams. According to Bayes’ theorem, given data \mathbf{D} , the posterior distribution of parameters $\boldsymbol{\theta}$ is proportional to the product of the prior distribution and the likelihood,

$$P(\boldsymbol{\theta}|\mathbf{D}) \propto P(\boldsymbol{\theta})P(\mathbf{D}|\boldsymbol{\theta}). \quad (17)$$

Here, the parameters we recover are

$$\boldsymbol{\theta} = \{A_b, A_v, A_l, \iota, \psi, \Phi_0\}. \quad (18)$$

As for the prior distribution, we assume $\log_{10} A_b$, $\log_{10} A_v$, $\log_{10} A_l$ follow $U[-10, 3]$, ψ and Φ_0 follow $U[0, 2\pi)$ and $\cos \iota$ follows $U[0, 1]$. After subtracting the waveform of extra polarizations $\mathbf{h}_e(\boldsymbol{\theta})$, the residual data \mathbf{d}_s ,

$$\mathbf{d}_s = \mathbf{d} - \mathbf{F}_e \mathbf{h}_e, \quad (19)$$

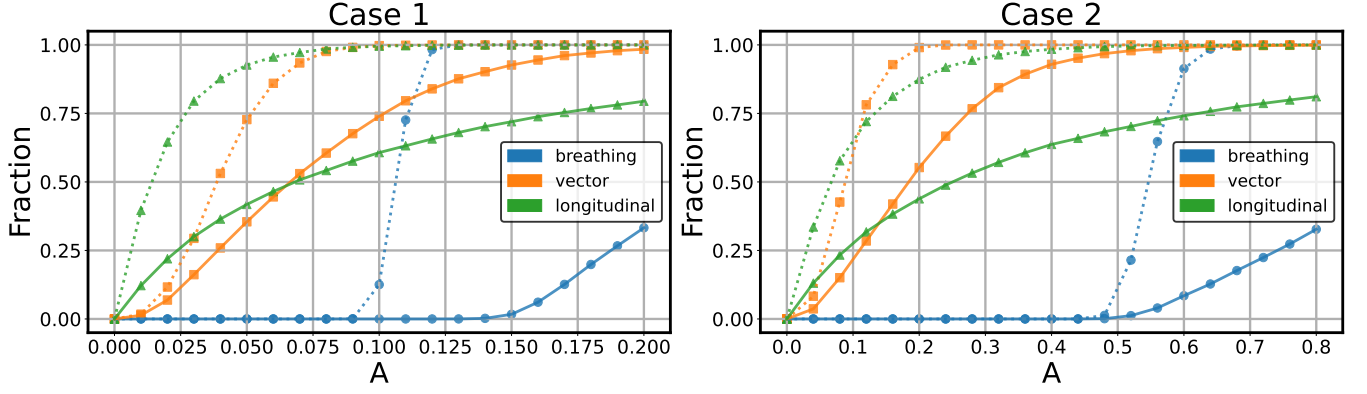


FIG. 3. Similar to Fig. 2. The results of 49 pulsars and 200 pulsars are denoted with solid lines and dashed lines respectively.

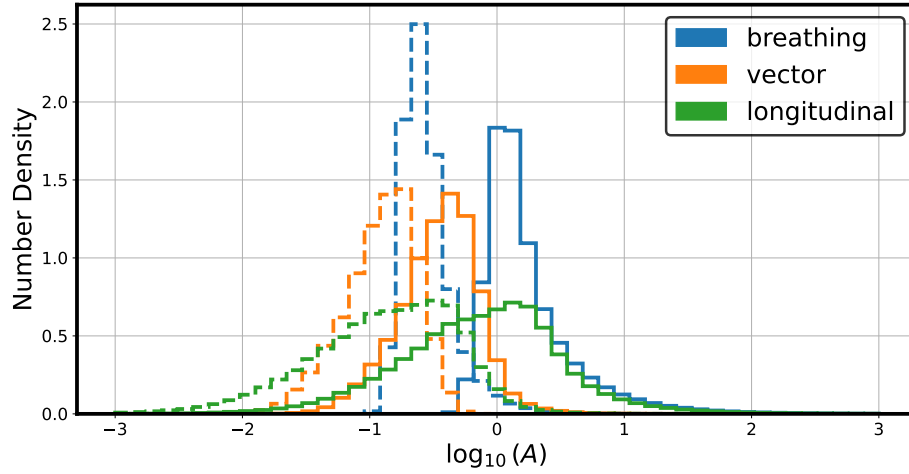


FIG. 4. Distribution of the logarithm of relative amplitude for specific extra modes to produce an injected SNR $\rho_{\text{inj}} = 22$ after projecting out all the other modes in 2×10^6 simulations. The results for Case 1 and Case 2 are denoted with dashed and solid lines respectively.

contain tensor modes and noise. Then, the corresponding streams after projection of \mathbf{U}^\dagger are

$$\tilde{\mathbf{d}}_s = \mathbf{U}^\dagger \mathbf{d}_s. \quad (20)$$

Now, under the assumption of Gaussian noise, the log-likelihood with null streams can be written as

$$\mathcal{L} \propto -\frac{1}{2} \sum_{k=3}^{49} \sum_n \frac{1}{\sigma_t^2} |\tilde{d}_{s,k}(t_n)|^2. \quad (21)$$

For all the simulations here, we fixed the source location to be $\theta = \pi/3$ and $\phi = -\pi/3$, and set $\iota = 3\pi/5$, $\psi = 4\pi/3$, $\Phi_0 = 1.2\pi$ for both Case 1 and Case 2. We inject the vector modes, breathing mode and longitudinal mode separately, assuming that the other modes are zero. For Case 1, the injection has $A_b = 1.2 \times 10^{-1}$, $A_v = 1.3 \times 10^{-2}$ and $A_l = 2.9 \times 10^{-4}$; for Case 2, the injection has $A_b = 6.6 \times 10^{-1}$, $A_v = 1.9 \times 10^{-2}$ and

$A_l = 1.1 \times 10^{-3}$. For all these injections, the relative amplitudes are chosen such that the corresponding injected SNR in the null streams is approximately 22, as in the previous section.

We make use of BILBY [67] with DYNESTY [68] as the sampler to do the parameter estimation. As pointed by O’Beirne *et al.* [41], there is degeneracy between ψ and Φ_0 in the parametrization model we use. Since, in this study, we are more interested in the relative amplitude and the inclination angle, we only show the posterior distribution of $\log_{10} A_b$, $\log_{10} A_v$, $\log_{10} A_l$ and ι in Fig. 5, after marginalizing over ψ and Φ_0 . It should be noted that there is strong degeneracy between the relative amplitude and the inclination angle in the waveform model. Therefore, we get a V-shape contour of the posterior distribution between ι and $\log_{10} A_b$ or $\log_{10} A_l$ when we inject only the breathing or longitudinal mode respectively. Thus, we cannot recover them separately. While for the

vector modes, since the vec-x mode and vec-y mode have different dependence on the inclination [see Eqs. (5) and (6)], this degeneracy can be broken.

V. DISCUSSIONS

In this work, we estimate the detectability of nontensorial polarizations with PTAs. We consider a circular SMBBH whose orbit barely evolves during the observation period. Two cases for the nontensorial polarizations are considered, where the dipole radiation dominates in Case 1 and the quadrupole radiation dominates in Case 2. Specifically, the waveforms for the two cases are parameterized in Eqs. (5) and (6) respectively. The strength of the extra polarizations is modulated by the relative amplitude A_e . For the PTA configuration, we consider 49 pulsars with the same timing variance $\sigma_t = 100$ ns and we assume a 9.5-year observation with 300 TOAs for each pulsar. The response of such a PTA to different polarizations is shown in Fig. 1.

We follow Zhu *et al.* [57] to construct null streams, in which all the tensor polarization signals are eliminated. Then we can quantify the deviation in the null streams to Gaussian noise to check if there is any evidence of nontensorial GW signals. With a frequentist analysis, we first estimate what fraction of the sky we can detect extra polarizations at $> 3\sigma$ confidence level for a specific strength. Equivalently, we estimate how likely we can detect nontensorial polarizations for a randomly distributed source using simulations. According to the results in Fig. 2, the values vary case by case in the simulations due to the random inclination and noise realization. Considering a fraction of 50%, i.e. when there is a 50% probability of finding evidence of nontensorial signals at $> 3\sigma$ confidence level, the median values are $A_b \approx 0.18$, $A_v \approx 0.08$, $A_l \approx 0.06$ for Case 1. For Case 2, the corresponding median values are $A_b \approx 0.96$, $A_v \approx 0.20$, $A_l \approx 0.22$. If we include more pulsars, the relative amplitude can be much lower.

We also project out all of the polarizations, but leave only one (breathing, vector, or longitudinal) mode in the null streams. In this case, we can claim evidence of a specific nontensorial polarization, that has not been projected out, if we find significant deviation in the null streams from Gaussian noise. By setting the injected

SNR to be 22, the median values for the relative amplitude are $A_b = 0.26$, $A_v = 0.13$, $A_l = 0.15$ for Case 1, and $A_b = 1.36$, $A_v = 0.37$, $A_l = 0.81$ for Case 2. The variance of the longitudinal mode is largest, since its response function strongly depends on the sky locations.

Lastly, we perform Bayesian analysis with the null streams to check how well we can recover the parameters of the model. Due to the degeneracy between the amplitude and the inclination, we can not recover them separately if we only inject breathing or longitudinal mode, while the combination of the vec-x mode and vec-y mode can break this degeneracy. As pointed out by O’Beirne *et al.* [41], the tensor modes can be mistaken as the breathing mode to some extent. But for null streams, this issue is alleviated since the tensor modes already vanish in the null streams.

In this work, we assume that the SMBBH is in a circular orbit, while for an eccentric binary, it can emit multiple harmonics of GWs. Including multiple harmonics can help break the degeneracy between the amplitude and the inclination. Furthermore, it is more realistic to consider the frequency evolution, so that the Earth term and the pulsar term have different frequency dependence [5]. Finally, we model the pulsar data with white noise only and assume that they are homogeneous. More realistic PTA data may impact the detectability of nontensorial polarizations. We leave these extensive studies to future work.

ACKNOWLEDGMENTS

We thank Nataliya Porayko and Lorenzo Speri for providing their codes to simulate pulsars distributed in the Galactic plane. We thank Kejia Lee, Zexin Hu and Ziming Wang for the helpful discussions. This work was supported by the China Postdoctoral Science Foundation (2021TQ0018, 2023M742297), the National SKA Program of China (2020SKA0120300), the National Natural Science Foundation of China (12250410246, 11991053, 11975027, 11721303), the Beijing Municipal Natural Science Foundation (1242018), the Max Planck Partner Group Program funded by the Max Planck Society, and the High-Performance Computing Platform of Peking University.

-
- [1] G. Agazie *et al.* (NANOGrav), *Astrophys. J. Lett.* **951**, L8 (2023), [arXiv:2306.16213 \[astro-ph.HE\]](#).
 - [2] J. Antoniadis *et al.* (EPTA), (2023), [arXiv:2306.16214 \[astro-ph.HE\]](#).
 - [3] D. J. Reardon *et al.*, *Astrophys. J. Lett.* **951**, L6 (2023), [arXiv:2306.16215 \[astro-ph.HE\]](#).
 - [4] H. Xu *et al.*, *Res. Astron. Astrophys.* **23**, 075024 (2023), [arXiv:2306.16216 \[astro-ph.HE\]](#).
 - [5] G. Janssen *et al.*, *PoS AASKA14*, 037 (2015), [arXiv:1501.00127 \[astro-ph.IM\]](#).
 - [6] A. Afzal *et al.* (NANOGrav), *Astrophys. J. Lett.* **951**, L11 (2023), [arXiv:2306.16219 \[astro-ph.HE\]](#).
 - [7] J. Antoniadis *et al.* (EPTA), (2023), [arXiv:2306.16227 \[astro-ph.CO\]](#).
 - [8] C. Smarra *et al.* (EPTA), (2023), [arXiv:2306.16228 \[astro-ph.HE\]](#).

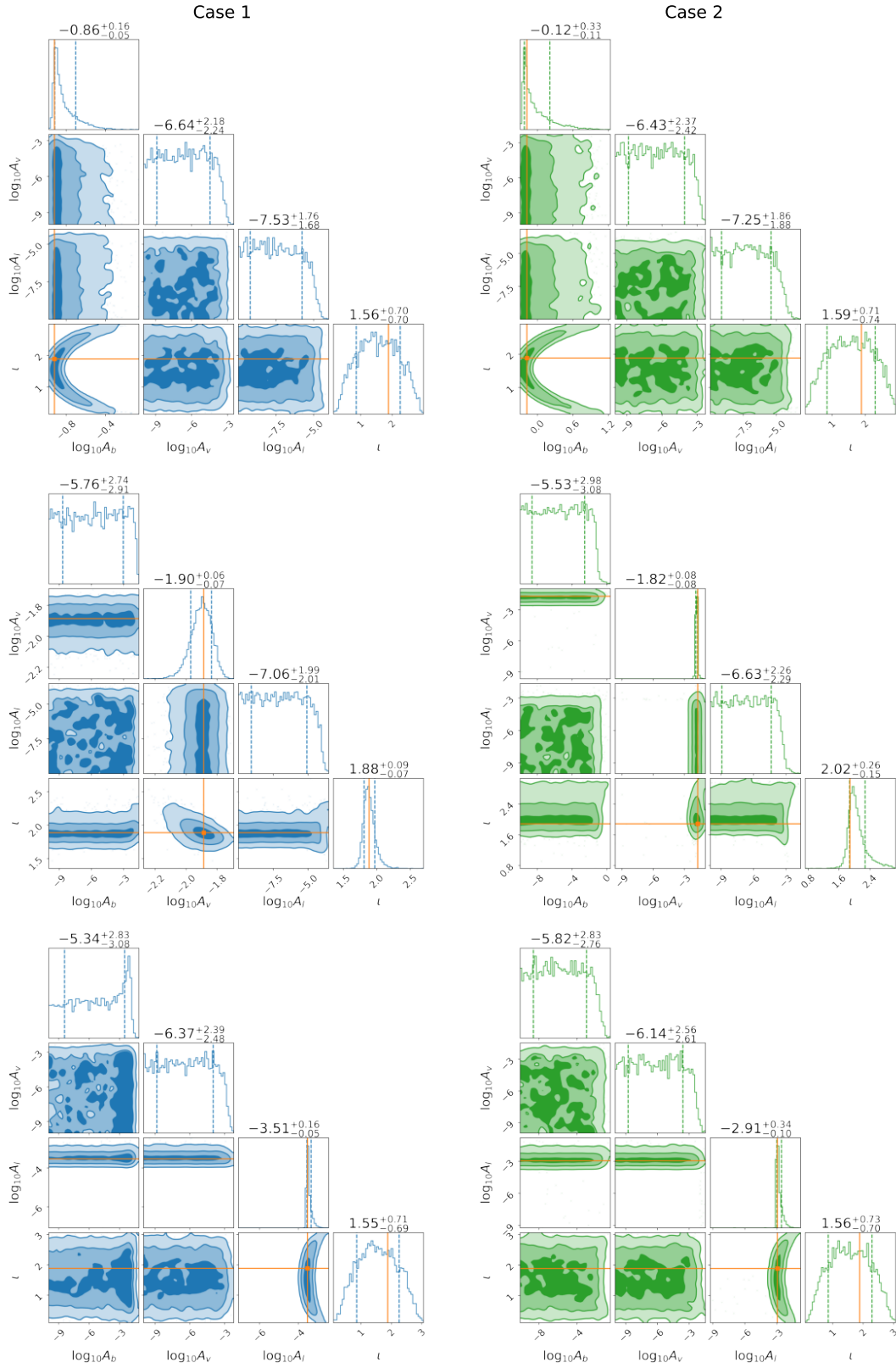


FIG. 5. Parameter estimation results with Bayesian inference (left panels for Case 1 and right panels for Case 2). The rows in order show injections of breathing, vector and longitudinal mode only. The orange dots/lines in the corner/histogram plots show the injected values.

- [9] S.-L. Li, L. Shao, P. Wu, and H. Yu, *Phys. Rev. D* **104**, 043510 (2021), [arXiv:2101.08012 \[astro-ph.CO\]](#).
- [10] C. Zhang, N. Dai, Q. Gao, Y. Gong, T. Jiang, and X. Lu, *Phys. Rev. D* **108**, 104069 (2023), [arXiv:2307.01093 \[gr-qc\]](#).
- [11] Z. Yi, Q. Gao, Y. Gong, Y. Wang, and F. Zhang, (2023), [arXiv:2307.02467 \[gr-qc\]](#).
- [12] Z. Yi, Z.-Q. You, and Y. Wu, (2023), [arXiv:2308.05632 \[astro-ph.CO\]](#).
- [13] S. Wang and Z.-C. Zhao, (2023), [arXiv:2307.04680 \[astro-ph.HE\]](#).
- [14] S. Wang, Z.-C. Zhao, J.-P. Li, and Q.-H. Zhu, (2023), [arXiv:2307.00572 \[astro-ph.CO\]](#).
- [15] D. M. Eardley, D. L. Lee, and A. P. Lightman, *Phys. Rev. D* **8**, 3308 (1973).
- [16] D. M. Eardley, D. L. Lee, A. P. Lightman, R. V. Wagoner, and C. M. Will, *Phys. Rev. Lett.* **30**, 884 (1973).
- [17] D. Liang, Y. Gong, S. Hou, and Y. Liu, *Phys. Rev. D* **95**, 104034 (2017), [arXiv:1701.05998 \[gr-qc\]](#).
- [18] T. Jacobson and D. Mattingly, *Phys. Rev. D* **70**, 024003 (2004), [arXiv:gr-qc/0402005](#).
- [19] D. Liang, R. Xu, X. Lu, and L. Shao, *Phys. Rev. D* **106**, 124019 (2022), [arXiv:2207.14423 \[gr-qc\]](#).
- [20] S. J. Chamberlin and X. Siemens, *Phys. Rev. D* **85**, 082001 (2012), [arXiv:1111.5661 \[astro-ph.HE\]](#).
- [21] A. Boitier, S. Tiwari, and P. Jetzer, *Phys. Rev. D* **103**, 064044 (2021), [arXiv:2011.13405 \[gr-qc\]](#).
- [22] A. Boitier, S. Tiwari, L. Philippoz, and P. Jetzer, *Phys. Rev. D* **102**, 064051 (2020), [arXiv:2008.13520 \[gr-qc\]](#).
- [23] Y. Hu, P.-P. Wang, Y.-J. Tan, and C.-G. Shao, *Phys. Rev. D* **106**, 024005 (2022), [arXiv:2205.09272 \[gr-qc\]](#).
- [24] R. C. Bernardo and K.-W. Ng, *Phys. Rev. D* **107**, 044007 (2023), [arXiv:2208.12538 \[gr-qc\]](#).
- [25] S. Hou, Y. Gong, and Y. Liu, *Eur. Phys. J. C* **78**, 378 (2018), [arXiv:1704.01899 \[gr-qc\]](#).
- [26] Y. Gong, S. Hou, E. Papantonopoulos, and D. Tzortzis, *Phys. Rev. D* **98**, 104017 (2018), [arXiv:1808.00632 \[gr-qc\]](#).
- [27] Y. Gong, S. Hou, D. Liang, and E. Papantonopoulos, *Phys. Rev. D* **97**, 084040 (2018), [arXiv:1801.03382 \[gr-qc\]](#).
- [28] Q. Liang and M. Trodden, *Phys. Rev. D* **104**, 084052 (2021), [arXiv:2108.05344 \[astro-ph.CO\]](#).
- [29] J. R. Gair, J. D. Romano, and S. R. Taylor, *Phys. Rev. D* **92**, 102003 (2015), [arXiv:1506.08668 \[gr-qc\]](#).
- [30] N. J. Cornish, L. O’Beirne, S. R. Taylor, and N. Yunes, *Phys. Rev. Lett.* **120**, 181101 (2018), [arXiv:1712.07132 \[gr-qc\]](#).
- [31] Z.-C. Chen, Y.-M. Wu, Y.-C. Bi, and Q.-G. Huang, (2023), [arXiv:2310.11238 \[astro-ph.CO\]](#).
- [32] G. Agazie *et al.*, (2023), [arXiv:2310.12138 \[gr-qc\]](#).
- [33] A. Sesana, A. Vecchio, and M. Volonteri, *Mon. Not. Roy. Astron. Soc.* **394**, 2255 (2009), [arXiv:0809.3412 \[astro-ph\]](#).
- [34] K. J. Lee, N. Wex, M. Kramer, B. W. Stappers, C. G. Bassa, G. H. Janssen, R. Karuppusamy, and R. Smits, *Mon. Not. Roy. Astron. Soc.* **414**, 3251 (2011), [arXiv:1103.0115 \[astro-ph.HE\]](#).
- [35] P. A. Rosado, A. Sesana, and J. Gair, *Mon. Not. Roy. Astron. Soc.* **451**, 2417 (2015), [arXiv:1503.04803 \[astro-ph.HE\]](#).
- [36] L. Z. Kelley, L. Blecha, L. Hernquist, A. Sesana, and S. R. Taylor, *Mon. Not. Roy. Astron. Soc.* **477**, 964 (2018), [arXiv:1711.00075 \[astro-ph.HE\]](#).
- [37] B. Bécsy, N. J. Cornish, and M. C. Digman, *Phys. Rev. D* **105**, 122003 (2022), [arXiv:2204.07160 \[gr-qc\]](#).
- [38] G. Agazie *et al.* (NANOGrav), *Astrophys. J. Lett.* **951**, L50 (2023), [arXiv:2306.16222 \[astro-ph.HE\]](#).
- [39] J. Antoniadis *et al.* (EPTA), (2023), [arXiv:2306.16226 \[astro-ph.HE\]](#).
- [40] R. Niu and W. Zhao, *Sci. China Phys. Mech. Astron.* **62**, 970411 (2019), [arXiv:1812.00208 \[gr-qc\]](#).
- [41] L. O’Beirne, N. J. Cornish, S. J. Vigeland, and S. R. Taylor, *Phys. Rev. D* **99**, 124039 (2019), [arXiv:1904.02744 \[gr-qc\]](#).
- [42] M. Isi and A. J. Weinstein, (2017), [arXiv:1710.03794 \[gr-qc\]](#).
- [43] B. P. Abbott *et al.* (LIGO Scientific, Virgo), *Phys. Rev. Lett.* **119**, 141101 (2017), [arXiv:1709.09660 \[gr-qc\]](#).
- [44] M. Isi, M. Pitkin, and A. J. Weinstein, *Phys. Rev. D* **96**, 042001 (2017), [arXiv:1703.07530 \[gr-qc\]](#).
- [45] T. Callister, A. S. Biscoveanu, N. Christensen, M. Isi, A. Matas, O. Minazzoli, T. Regimbau, M. Sakellariadou, J. Tasson, and E. Thrane, *Phys. Rev. X* **7**, 041058 (2017), [arXiv:1704.08373 \[gr-qc\]](#).
- [46] B. P. Abbott *et al.* (LIGO Scientific, Virgo), *Phys. Rev. Lett.* **120**, 201102 (2018), [arXiv:1802.10194 \[gr-qc\]](#).
- [47] Y. Hagihara, N. Era, D. Iikawa, A. Nishizawa, and H. Asada, *Phys. Rev. D* **100**, 064010 (2019), [arXiv:1904.02300 \[gr-qc\]](#).
- [48] P. T. H. Pang, R. K. L. Lo, I. C. F. Wong, T. G. F. Li, and C. Van Den Broeck, *Phys. Rev. D* **101**, 104055 (2020), [arXiv:2003.07375 \[gr-qc\]](#).
- [49] I. C. F. Wong, P. T. H. Pang, R. K. L. Lo, T. G. F. Li, and C. Van Den Broeck, (2021), [arXiv:2105.09485 \[gr-qc\]](#).
- [50] R. Abbott *et al.* (LIGO Scientific, Virgo), *Phys. Rev. D* **103**, 122002 (2021), [arXiv:2010.14529 \[gr-qc\]](#).
- [51] R. Abbott *et al.* (LIGO Scientific, VIRGO, KAGRA), (2021), [arXiv:2112.06861 \[gr-qc\]](#).
- [52] J. Hu, D. Liang, and L. Shao, (2023), [arXiv:2310.01249 \[gr-qc\]](#).
- [53] C. Zhang, Y. Gong, D. Liang, and C. Zhang, *Phys. Rev. D* **105**, 104062 (2022), [arXiv:2102.03972 \[gr-qc\]](#).
- [54] Y. Guersel and M. Tinto, *Phys. Rev. D* **40**, 3884 (1989).
- [55] S. Chatterji, A. Lazzarini, L. Stein, P. J. Sutton, A. Searle, and M. Tinto, *Phys. Rev. D* **74**, 082005 (2006), [arXiv:gr-qc/0605002](#).
- [56] K. Chatziioannou, N. Yunes, and N. Cornish, *Phys. Rev. D* **86**, 022004 (2012), [Erratum: *Phys. Rev. D* **95**, 129901 (2017)], [arXiv:1204.2585 \[gr-qc\]](#).
- [57] X.-J. Zhu, L. Wen, G. Hobbs, Y. Zhang, Y. Wang, D. R. Madison, R. N. Manchester, M. Kerr, P. A. Rosado, and J.-B. Wang, *Mon. Not. Roy. Astron. Soc.* **449**, 1650 (2015), [arXiv:1502.06001 \[astro-ph.IM\]](#).
- [58] X. Zhu, L. Wen, J. Xiong, Y. Xu, Y. Wang, S. D. Mohanty, G. Hobbs, and R. N. Manchester, *Mon. Not. Roy. Astron. Soc.* **461**, 1317 (2016), [arXiv:1606.04539 \[astro-ph.IM\]](#).
- [59] J. Goldstein, J. Veitch, A. Sesana, and A. Vecchio, *Mon. Not. Roy. Astron. Soc.* **477**, 5447 (2018), [arXiv:1712.03975 \[astro-ph.IM\]](#).
- [60] J. M. Goldstein, A. Sesana, A. M. Holgado, and J. Veitch, (2018), [10.1093/mnras/stz420](#), [arXiv:1812.02670 \[astro-ph.IM\]](#).
- [61] J. D. Romano and N. J. Cornish, *Living Rev. Rel.* **20**, 2 (2017), [arXiv:1608.06889 \[gr-qc\]](#).

- [62] J. D. Romano and B. Allen, (2023), [arXiv:2308.05847 \[gr-qc\]](#).
- [63] J. P. W. Verbiest *et al.*, *Mon. Not. Roy. Astron. Soc.* **458**, 1267 (2016), [arXiv:1602.03640 \[astro-ph.IM\]](#).
- [64] R. N. Manchester, G. B. Hobbs, A. Teoh, and M. Hobbs, *Astron. J.* **129**, 1993 (2005), [arXiv:astro-ph/0412641](#).
- [65] H. Takeda, A. Nishizawa, Y. Michimura, K. Nagano, K. Komori, M. Ando, and K. Hayama, *Phys. Rev. D* **98**, 022008 (2018), [arXiv:1806.02182 \[gr-qc\]](#).
- [66] L. Speri, N. K. Porayko, M. Falxa, S. Chen, J. R. Gair, A. Sesana, and S. R. Taylor, *Mon. Not. Roy. Astron. Soc.* **518**, 1802 (2022), [arXiv:2211.03201 \[astro-ph.HE\]](#).
- [67] G. Ashton *et al.*, *Astrophys. J. Suppl.* **241**, 27 (2019), [arXiv:1811.02042 \[astro-ph.IM\]](#).
- [68] J. S. Speagle, *Mon. Not. Roy. Astron. Soc.* **493**, 3132 (2020), [arXiv:1904.02180 \[astro-ph.IM\]](#).